Computational Study of Swallowing Disorders

Imran Rizki Putranto

Abstract

This study investigates the application of Smoothed Particle Hydrodynamics (SPH) to simulate the swallowing process, which is of significant interest in understanding and diagnosing dysphagia. This research focuses on the development and validation of a two-dimensional model for simulating bolus flow and its interaction with anatomical structures during swallowing. The model utilised the Weakly Compressible SPH (WCSPH) approach and incorporated boundary conditions derived from two-dimensional videofluoroscopic swallowing study (VFSS) data. The code was implemented in Python using the NumPy, Matplotlib and Scikit-Learn libraries, and GPU acceleration was achieved using the Numba library. The code was validated by comparing the results of one-dimensional function approximations and a two-dimensional dam break problem against numerical and experimental data available in literature. The results of the two-dimensional swallowing simulation revealed the ability of SPH to capture the overall bolus flow during the swallowing process. However, the simulation exposed some limitations, such as slight fluid compression and challenges in conserving the bolus surface area. Due to the swallowing process inherently being a three-dimensional process with complex interactions with surrounding tissue, several assumptions made led to relatively inaccurate results. Despite these limitations, this study demonstrates the potential of SPH in modelling the swallowing process and lays the groundwork for future research involving more advanced and accurate three-dimensional incompressible models and potential medical applications to aid clinicians with the diagnosis and treatment of dysphagia.

Supervised by Dr A. Gambaruto

Department of Mechanical Engineering
University of Bristol
2023

Declaration

This project report is submitted towards an application for a degree in Mechanical Engineering at the University of Bristol. The report is based upon independent work by the candidate. All contributions from others have been acknowledged and the supervisor is identified on the front page. The views expressed within the report are those of the author and not of the University of Bristol.

I hereby assert my right to be identified as the author of this report. I give permission to the University of Bristol Library to add this report to its stock and to make it available for consultation in the library, and for inter-library lending for use in another library. It may be copied in full or in part for any bona fide library or research worker on the understanding that users are made aware of their obligations under copyright legislation.

I hereby declare that the above statements are true.

Acknowledgements

Contents

1 Introduction

Swallowing constitutes an indispensable aspect of life, facilitating the safe and efficient consumption of food and liquids and serving as a critical process for sustaining life. The pleasure of eating and drinking plays a significant role in an individual's perception of their overall well-being and happiness. Swallowing represents a highly intricate and robust mechanism involving the central and peripheral nervous systems, the interaction between 25 pairs of muscles and intact anatomical structures of the upper aerodigestive tract and oesophagus [1]. Unfortunately, some individuals suffer from complications that do not allow them to swallow food and fluids properly. *Dysphagia* is a medical term that describes difficulty swallowing and is predominantly observed in the older population. This condition can arise from structural and functional abnormalities and a wide variety of diseases and disorders. Moreover, dysphagia is linked with other health complications and may lead to severe consequences if left undiagnosed and untreated.

The swallowing process has proven to be a challenge to model mathematically due to its swiftness and complexity. Previous studies by Nicosia et al. [2] [3] have attempted to analyse the bolus flow. However, the use of simplified geometry to model anatomical structures in these studies do not make them viable due to the intricacies of the boundaries, which involve the rapid interaction with the food bolus. Other studies have attempted to improve upon the anatomical geometry. Sonomura et al. [4] utilised an Eulerian volume-of-fluid method. Unfortunately, the assumptions made during their study may have affected the accuracy of their results. Consequently, more accurate, efficient, and comprehensive mathematical models that can realistically simulate the human swallowing process still need to be developed.

1.1 Aims and Objectives

The present study investigates the potential and capabilities of Smoothed Particle Hydrodynamics (SPH) as a numerical simulation technique, aiming to simulate the human swallowing process using SPH in Python. The SPH algorithm was implemented using the NumPy, Matplotlib and Scikit-Learn libraries to achieve this. The Numba library was also used for GPU acceleration, which sped up the simulations by 30 to 40 times. Several SPH benchmark tests were conducted and subsequently validated to determine the reliability of the method. Processed medical images of the bolus at different time steps were obtained from Videofluoroscopic Swallow Studies (VFSS). These images were then interpolated to model the boundaries for the SPH simulation. A successful numerical simulation of the swallowing process could provide valuable insights into the intricate dynamics and interactions within the upper aerodigestive tract, enabling healthcare professionals to assess the swallowing ability of an individual objectively.

2 Background and Motivations

2.1 Stages of Normal Swallowing

Swallowing constitutes an exceptionally rapid and intricate procedure continuously being subjected to research. The swallowing process can be categorised into three primary stages: oral, pharyngeal, and oesophageal. The oral stage can be divided into the oral preparatory and oral propulsive stages, yielding a comprehensive four-stage process commonly used to describe the typical human swallowing process [5]. In the oral preparatory stage, food and liquid are chewed, combined with saliva, and formed into a bolus. The oral propulsive stage involves the propulsion of the bolus by the tongue and the elevation of the soft palate to expand the pharyngeal space to accommodate the bolus passage. The pharyngeal stage represents a reflex stage necessitating the coordination between respiration and swallowing. Numerous processes occur in rapid succession within this stage, with vocal fold adduction providing the primary protective mechanism against aspiration. This causes a period of apnoea lasting anywhere between 0.3 to 2.5 seconds. Any reduction in the effectiveness of these processes may lead to aspiration. Finally, in the oesophageal stage, peristalsis propels the bolus to the oesophageal sphincter [6].

2.2 A Background Into Dysphagia

Dysphagia can be classified into two primary types, oropharyngeal and oesophageal [7], which occur in the oropharynx and oesophagus respectively (see Figure 1). Oropharyngeal dysphagia primarily stems from complications in the pharyngeal swallowing stage. As previously mentioned, dysphagia can arise from various diseases and disorders, including neurological conditions, congenital and developmental conditions, physical obstructions such as tumours, and muscular conditions. Nevertheless, neurological disorders such as stroke, dementia, Parkinson's disease and neuromuscular diseases are the most common causes.
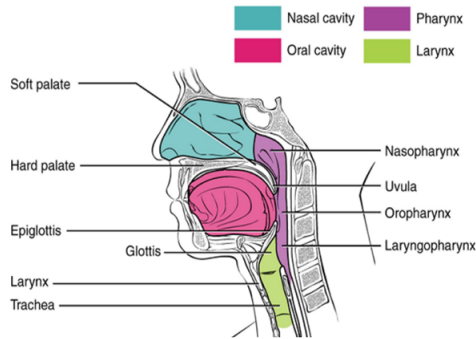

Figure 1: Anatomy of the Mouth, Pharynx and Oesophagus [5]

Dysphagia can have significant physical and psychological implications. It may impact an individual's quality of life and lead to dehydration, malnutrition, and aspiration pneumonia, which may result in mortality. Conservative estimates suggest that the rate of occurrence of dysphagia may be [8]:

- about 3% in U.S. inpatients aged 45 years or older to as high as 22% in adults over 50 years of age;
- as high as 30% in elderly populations receiving inpatient medical treatment;
- up to 68% for residents in long-term care settings and;
- 13% to 38% among elderly individuals who are living independently.

2.3 Diagnosis and Current Treatments For Dysphagia

VFSS is one of the more popular ways clinicians evaluate an individual's swallowing capability. VFSS, also referred to as modified barium swallow (MBS), is a radiographic procedure involving real-time imaging of the swallowing process via a fluoroscope while the patient consumes various food and liquids with different consistencies mixed with barium sulfate. This enables the visualisation of the bolus as it traverses the oral cavity, pharynx, and oesophagus. It also delivers a comprehensive assessment of the swallowing process, including oral and pharyngeal transit time, coordination, and efficiency, as well as the identification of any abnormalities. This data can be used to diagnose dysphagia and identify any possible causes.

However, most data is assessed subjectively and depends on individual clinicians, which presents a need to develop a standard and more objective method to assess this data. It was found that trained clinical evaluators frequently reported inconsistent results of their assessments, with the unanimous agreement of VFSS interpretation only happening 28% of the time [9]. In addition, conducting extensive and possibly invasive testing, such as oesophageal manometry, may be challenging and unsafe due to the older age of patients suffering from dysphagia. As a result, current treatments may not be tailored to the specific individual and may increase the risk of complications. Numerical simulations would complement existing assessment methods by offering a quantitative and detailed analysis of the swallowing process, highlighting parameters such as pressures and velocities of the bolus as it travels down the upper aerodigestive tract. This would enable clinicians to identify specific abnormalities and dysfunctions with greater precision,

leading to more targeted treatment plans and potentially reducing the need for repetitive or invasive diagnostic procedures, ultimately enhancing patient care and outcomes.

Different approaches to treating dysphagia depend on the underlying cause and severity of the condition. Swallowing therapy is a common approach to treating dysphagia. A speech-language pathologist can provide exercises and techniques to improve swallowing function [10], potentially incorporating strategies such as altering head position during swallowing and exercises to strengthen the muscles involved in the swallowing process [11]. Modifying the texture and consistency of the ingested food and beverages is another treatment option. These alterations may include pureeing solid foods or thickening liquids to prevent aspiration [12]. The International Dysphagia Diet Standardisation Initiative (IDDSI) Framework provides a common terminology to describe food textures and drink thickness, comprising a continuum of eight levels to measure against [13]. This facilitates clear communication to ensure the food and drinks have a safe texture and consistency. In more severe cases, surgical interventions may be necessary.

3 Smoothed Particle Hydrodynamics

Smoothed Particle Hydrodynamics (SPH) is a mesh-free, Lagrangian numerical simulation technique extensively employed in computational fluid dynamics to model complex fluid flow. It was simultaneously developed in 1977 by Gingold and Monaghan [14] to simulate astrophysical phenomena and by Lucy [15] to study a rotating polytropic fluid undergoing fission to produce a binary system. Fundamentally, SPH represents the fluid as a collection of particles that move through space and interact. The fluid motion is approximated through the governing equations of motion for fluid flow. Each particle possesses properties including mass, density and pressure and interacts with other particles within a radius governed by a smoothing or kernel function; hence the term 'Smoothed'.

Although they require relatively more computational power than mesh-based methods, mesh-free approaches such as SPH offer key advantages, such as the ability to handle complex geometries and moving boundaries better and being more robust in conserving mass and momentum. SPH is also recognised for its capability to simulate high-velocity flows and large deformations with relative ease. Consequently, a simulation of the swallowing process would be better represented using SPH.

3.1 Discrete Approximations to a Continuous Field

3.1.1 Continuous Approximation

The core of all SPH formalisms originates from the integral identity below:

$$a(\mathbf{x}) = \int_{\Omega} a(\mathbf{x'})\delta(\mathbf{x} - \mathbf{x'})dV' \tag{1}$$

Where $a(\mathbf{x})$ is an arbitrary function defined within the domain Ω, $\delta(\mathbf{x} - \mathbf{x'})$ is the Dirac delta function and dV' is the particle volume. Vector $\mathbf{x}$ denotes the coordinates of the specific point in Ω and $\mathbf{x'}$ is the variable of integration. The Dirac delta function is given as:

$$\delta(\mathbf{x} - \mathbf{x'}) = \begin{cases} 1, & \text{if } \mathbf{x} = \mathbf{x'} \\ 0, & \text{otherwise} \end{cases} \tag{2}$$

In SPH, the Dirac delta function is substituted by a smoothing or kernel function, $W(\mathbf{x} - \mathbf{x'}, h)$, where h is the smoothing length and controls the amount of smoothing and, as a result, the extent to which the function $a(\mathbf{x})$ at position $\mathbf{x}$ is influenced by its neighbours [16]. In essence, the smoothing effect intensifies as the smoothing length increases. Various smoothing kernels have been developed over the years, each

presenting its benefits and drawbacks. However, all kernels must satisfy several requirements, as compiled and summarised by Koschier et al. [16] and Liu [17]. Apart from these constraints, one can design kernels for specific purposes. Gingold and Monaghan initially selected the Gaussian kernel [14]:

$$W(\mathbf{r}, h) = \pi^{-\frac{d}{2}} h^{-d} e^{-q^2} \tag{3}$$

Where $q = \frac{\|\mathbf{r}\|}{h}$ and d is the number of spatial dimensions. $\mathbf{r}$ is the distance vector between two particles. The smoothing length, h, typically has a value of 1.2 to 1.3 times the initial particle spacing, dx [18].

The Gaussian kernel is widely regarded as the default choice due to its stability and accuracy. It can be differentiated as many times as required and is sufficiently smooth, even for higher-order derivatives. However, its value does not truly reach zero unless its support domain approaches infinity, meaning that it lacks compact support - one of the requirements of a kernel function. Hence, it is not a suitable choice for simulations prioritising computational efficiency. One of the most widely used kernels is the cubic spline kernel originally proposed by Monaghan and Lattanzio [19] due to its balance between computational cost and accuracy. Several formulations of the cubic spline kernel throughout SPH literature are parameterised differently with respect to h. The version proposed by Monaghan and Lattanzio is:

$$W(\mathbf{r}, h) = \sigma_d \begin{cases} 1 - \frac{3}{2}q^2(1 - \frac{q}{2}), & 0 \le q \le 1 \\ \frac{1}{4}(2-q)^3, & 1 < q \le 2 \\ 0, & \text{otherwise} \end{cases} \tag{4}$$

The kernel normalisation factors for their respective dimensions, $d = 1, 2, 3$, are $\sigma_1 = \frac{4}{3h}$, $\sigma_2 = \frac{40}{7\pi h^2}$, and $\sigma_3 = \frac{8}{\pi h^3}$. The cubic spline kernel is highly popular as it closely resembles a Gaussian function and has a narrower compact support, making it less computationally expensive. However, its second derivative is a piecewise linear function, making it less stable compared to other higher-order kernels. Other kernels, such as the Quintic spline [17] and Wendland [20], were developed to improve specific properties like smoothness and computational efficiency. Figure 2 below illustrates how the values of the cubic spline kernel and its first-order derivative vary against different values of $\mathbf{r}$ for a given smoothing length.
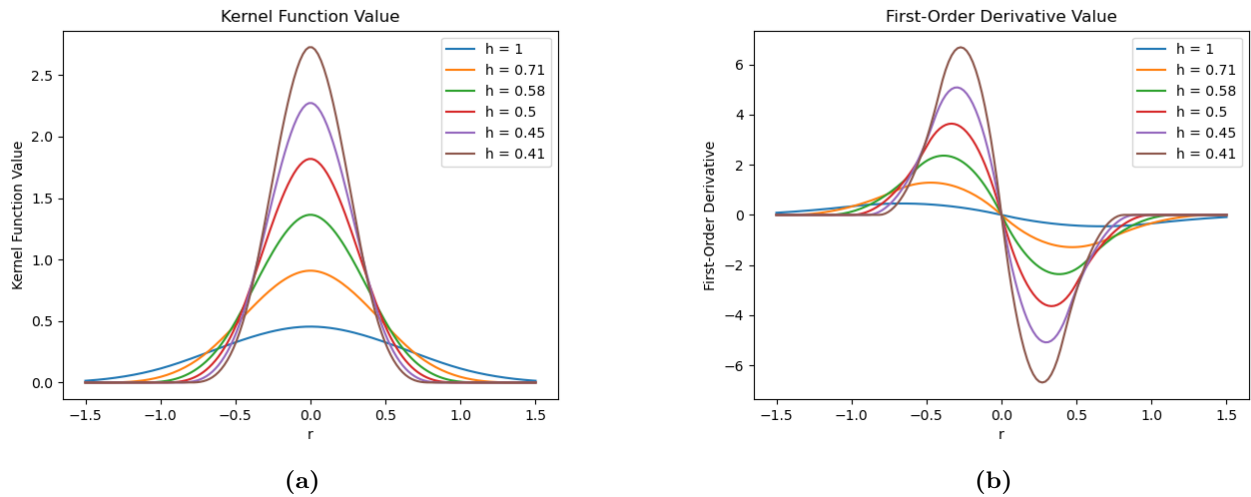

(a)

(b)

Figure 2: (a) Cubic Spline Kernel Function, (b) First-Order Derivative

3.1.2 Discretisation

Representing dV' from Equation 1 as $\frac{m_j}{\rho_j}$, the discrete SPH approximation of a function becomes:

$$a(\mathbf{x}_i) \approx \sum_j \frac{m_j}{\rho_j} a(\mathbf{x}_j) W(\mathbf{x}_i - \mathbf{x}_j, h) \tag{5}$$

Where m and ρ are the mass and density of particle j, respectively, a represents an arbitrary function, $\mathbf{x}_i$ and $\mathbf{x}_j$ denote the positions of particles i and j, and $W(\mathbf{x}_i - \mathbf{x}_j, h)$ is the smoothing kernel. The indices i and j serve as particle identifiers, with i as the particle of interest and j as its neighbouring particle. To improve readability, $W(\mathbf{x}_i - \mathbf{x}_j, h)$ has been abbreviated to W_{ij} in subsequent equations.

3.2 Discretisation of Differential Operators

For SPH to be useful for simulating fluid flows, the spatial derivatives of any given quantity must also possess a suitable approximation. The discretisation of the gradient of a scalar field can be expressed as:

$$\nabla a(\mathbf{x}_i) \approx \sum_j \frac{m_j}{\rho_j} a(\mathbf{x}_j) \nabla W_{ij} \tag{6}$$

Where ∇ is the differential operator. An alternative, symmetric expression is:

$$\nabla a(\mathbf{x}_i) \approx \rho_i \sum_j m_j \left(\frac{a(\mathbf{x}_i)}{\rho_i^2} + \frac{a(\mathbf{x}_j)}{\rho_j^2} \right) \nabla W_{ij} \tag{7}$$

This form is commonly used to discretise the pressure gradient term in the Navier-Stokes equation, as it is pairwise symmetric and thus ensures the conservation of momentum [21]. The discrete approximations for the divergence, curl and Laplacian operators of a function are shown by Equations 8, 9 and 10:

$$\nabla \cdot a(\mathbf{x}_i) \approx \sum_j \frac{m_j}{\rho_j} a(\mathbf{x}_j) \cdot \nabla W_{ij} \tag{8}$$

$$\nabla \times a(\mathbf{x}_i) \approx \sum_j \frac{m_j}{\rho_j} a(\mathbf{x}_j) \nabla \times W_{ij} \tag{9}$$

$$\nabla^2 a(\mathbf{x}_i) \approx \sum_j \frac{m_j}{\rho_j} a(\mathbf{x}_j) \nabla^2 W_{ij} \tag{10}$$

Second-order derivatives tend to be poorly estimated using SPH, which creates challenges when discretising the viscosity term of the Navier-Stokes equation. Improved formulations to discretise the Laplacian have been proposed in various literature and applied to the viscosity term.

3.3 Governing Equations of Motion

The governing equations for fluid motion are the continuity and Navier-Stokes equations, which describe the conservation of mass and linear momentum in a fluid. The Lagrangian form of these equations are shown in Equations 11 and 12 respectively:

$$\frac{D\rho}{Dt} = -\rho \nabla \cdot \mathbf{v} \tag{11}$$

Where $\frac{D\rho}{Dt}$ is the rate of change of density and $\mathbf{v}$ is the velocity.

$$\frac{D\mathbf{v}}{Dt} = -\frac{1}{\rho} \nabla p + \nu \nabla^2 \mathbf{v} + \mathbf{g} \tag{12}$$

Where $\frac{D\mathbf{v}}{Dt}$ denotes the acceleration, ∇p represents the pressure gradient, ν is the kinematic viscosity, ∇^2 is the Laplacian and $\mathbf{g}$ is the gravitational acceleration. In most cases, the Navier-Stokes equation is difficult to solve analytically and requires numerical methods such as SPH to obtain approximate solutions.

3.4 Density Approximation

The most common approach to estimate particle densities is by summing over the particles:

$$\rho_i = \sum_j m_j W_{ij} \tag{13}$$

Where ρ_i is the density of particle i, m_j is the mass of particle j and W_{ij} is the kernel function. However, due to the lack of particles at surfaces, this equation may underestimate the densities for particles situated at surfaces or edges due to particle deficiency [22], leading to inaccurate pressure and force calculations. Figure 3 provides a visual representation of this phenomenon.
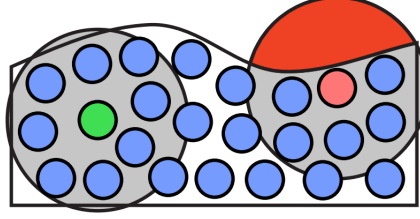

Figure 3: Particle Deficiency Issue Highlighted By the Red Particle [16]

An alternative approach is to assign each particle with an initial density, ρ_0, and approximate the rate of change of the density at each time step using the discretisation of the continuity equation:

$$\frac{D\rho_i}{Dt} = \sum_j m_j \mathbf{v}_{ij} \cdot W_{ij} \tag{14}$$

Where $\frac{D\rho_i}{Dt}$ is the rate of change of density and $\mathbf{v}_{ij}$ is the difference in velocity of particles i and j.

3.5 Discretising the Navier-Stokes Equation

3.5.1 Inviscid Navier-Stokes Equation

As mentioned in Section 3.2, Equation 7 is commonly used as an estimator for the pressure gradient in the Navier-Stokes equation. The discretised inviscid Navier-Stokes equation has the form:

$$\frac{D\mathbf{v}_i}{Dt} = -\sum_j m_j \left(\frac{p_i}{\rho_i^2} + \frac{p_j}{\rho_j^2} \right) \nabla W_{ij} + \mathbf{g} \tag{15}$$

Where $\frac{D\mathbf{v}_i}{Dt}$ is the acceleration of particle i, p_i and p_j are the pressures of particles i and j respectively and $\mathbf{g}$ is the gravitational acceleration. Other formulations exist, but the formulation above is more widely used due to its symmetric form, which consequently conserves momentum.

3.5.2 Viscosity Term

There are scenarios where the viscosity term in the Navier-Stokes equation cannot be dropped in cases involving viscous-dominated flows. However, discretising second-order derivatives in SPH is undesirable as its interpolation is more susceptible to errors at lower resolutions, resulting in larger errors than discretisations of first-order derivatives [23]. Monaghan derived an artificial viscosity term for the discretisation of the Navier-Stokes equation [24]:

$$\frac{D\mathbf{v}_i}{Dt} = -\sum_j m_j \left(\frac{p_i}{\rho_i^2} + \frac{p_j}{\rho_j^2} + \Pi_{ij} \right) \nabla W_{ij} + \mathbf{g} \tag{16}$$

Where Π_{ij} is the artificial viscosity term with the expression:

$$\Pi_{ij} = \begin{cases} \frac{-\alpha \bar{c}_{ij} \mu_{ij} + \beta \mu_{ij}^2}{\bar{\rho}_{ij}}, & < 0 \\ 0, & \geq 0 \end{cases} \tag{17}$$

μ_{ij} is an expression which has the form:

$$\mu_{ij} = \frac{h \mathbf{v}_{ij} \cdot \mathbf{r}_{ij}}{||\mathbf{r}_{ij}^2|| + 0.01 h^2} \tag{18}$$

In these expressions, the notations $\mathbf{A}_{ij} = \mathbf{A}_i - \mathbf{A}_j$ and $\overline{A}_{ij} = \frac{(A_i + A_j)}{2}$. The term $||\mathbf{r}_{ij}^2||$ is the Euclidean distance between two particles. The term $\bar{c}_{ij}$ is the average between the speed of sounds of particles i and j, c_i and c_j. These can be calculated from the expression:

$$c_i = c_0 \left(\frac{\rho_i}{\rho_0} \right)^{\left(\frac{\gamma - 1}{2} \right)} \tag{19}$$

Where c_0 is the artificial speed of sound and $\gamma = 7$ in the case of fluids. The artificial viscosity term, initially devised for shock wave handling and numerical stability, consists of a linear term controlled by α and a quadratic term controlled by β. These terms approximate shear and bulk viscosities and handle high Mach number shocks. However, the quadratic term contributes little to the present study and thus, β was set to zero in the following simulations. A limitation of this expression is the need to adjust α and β based on the problem. Efforts have been made to correlate artificial and physical viscosities through empirical results, but these depend on the specific problem and are not universally applicable. Despite being widely used in modelling the viscosity, the formula has shown lesser accuracy for low Reynolds number flow velocity profiles [23]. However, it ensures the conservation of angular momentum.

3.6 Equation of State - Weakly Compressible Approach

Since the inception of SPH, various expressions relating pressure to density have been formulated. When incompressibility is a requirement, the Pressure Poisson equation can be solved:

$$\nabla^2 p^{n+1} = \frac{\rho}{\Delta t} \nabla \cdot \mathbf{u}^* \tag{20}$$

Where $\mathbf{u}^*$ is a predictor velocity. Nonetheless, solving the Pressure Poisson equation might demand a substantial amount of computational time compared to other equations. In contrast, scenarios that allow compressibility may employ the modified ideal gas equation proposed by Desbrun [25]:

$$p = k(\rho - \rho_0) \tag{21}$$

Where k is a constant and ρ_0 is the rest density. While the ideal gas approach is easier to implement and less computationally expensive, it results in high compressibility, which is undesirable in specific scenarios, such as those in the present study. The Weakly Compressible SPH approach (WCSPH) [26] employs the Tait equation, which enforces low density fluctuations while being relatively efficient to compute:

$$p = B \left[\left(\frac{\rho}{\rho_0} \right)^\gamma - 1 \right] \tag{22}$$

Where p is the pressure, B is a constant that governs the relative density fluctuations $\frac{\Delta \rho}{\rho_0}$, $\gamma = 7$ for fluids, ρ_0 is the rest density and ρ is the particle density. Typically, a maximum density fluctuation of 0.01 or 1% is allowed, giving $\frac{\Delta \rho}{\rho_0} = 0.01$. To enforce this condition, B was given the expression:

$$B = \frac{\rho_0 c_0^2}{\gamma} \tag{23}$$

Where c_0 is the artificial speed of sound of the fluid and is approximately ten times the maximum or reference velocity, v_f, of the fluid flow:

$$v_f = \sqrt{2gH} \tag{24}$$

Where g is the gravitational acceleration and H is the height of the fluid. As an example, for a column of water $1m$ tall, the reference velocity is approximately $4.43m/s$, the artificial speed of sound is $44.3m/s$, and B is $280kPa$ assuming $\rho_0 = 1000kg/m^3$ and $\gamma = 7$.

3.7 Boundary Conditions

One of the main problems in SPH is the modelling of boundaries. Several approaches have been developed over time, such as the Lennard-Jones Boundary Force [22], Ghost Particle method [27] and Dynamic Boundary Particles method [28]. The simulations in this study employed lines of fixed particles as proposed by Gotoh and Sakai [29]. The densities and pressures of the wall particles were calculated alongside the fluid particles at each time step. Consequently, as the fluid particles approach the wall particles, the latter's densities and pressures would increase, thereby repelling the fluid particles.
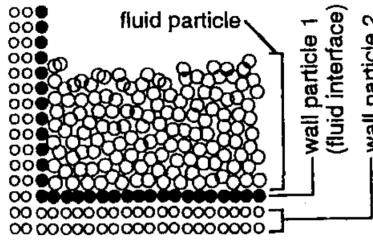

Figure 4: Wall Boundary Particle Arrangement [29]

To ensure sufficient repulsive forces, several layers of ghost particles were added outside the first layer, as depicted in Figure 4. This addressed the particle deficiency issue mentioned in Section 3.4 above. Without these additional wall particles, the densities and pressures of the particles in the first layer would be underestimated, potentially being recognised as a free surface and leading to boundary penetration.

3.8 Time Integration

The SPH discretisation of the Navier-Stokes equation yields a system of ODEs, which must be numerically integrated with time to obtain the velocity and position of each particle at each time step. One of the simplest integration schemes, the Euler forward scheme, is relatively easy to implement and computationally inexpensive. However, its first-order accuracy can lead to significant numerical errors in the long term and poor energy conservation properties. The Runge-Kutta fourth-order (RK4) method, another widely used explicit scheme, enhances accuracy by taking four estimates of the time derivative within each time step, making it fourth-order accurate. This results in considerably reduced numerical errors, albeit at a higher computational cost.
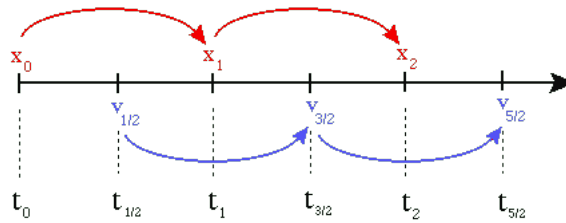

Figure 5: Leapfrog Integration Scheme

The Leapfrog integration scheme, a method commonly employed in particle-based methods, was used in this study. As it is an explicit, second-order accurate, and symplectic scheme, it conserves energy, provided the time step is small enough for stability. The scheme derives its name from velocities being updated at half time steps, while positions are updated at integer steps - effectively leaping over each other. A visualisation can be seen in Figure 5. The equations making up the scheme are:

$$\mathbf{v}_i^{n+\frac{1}{2}} = \mathbf{v}_i^{n-\frac{1}{2}} + \left(\frac{d\mathbf{v}_i}{dt}\right)^n \Delta t \tag{25}$$

$$\mathbf{v}_i^{n+1} = \mathbf{v}_i^{n+\frac{1}{2}} + \left(\frac{d\mathbf{v}_i}{dt}\right)^n \frac{\Delta t}{2} \tag{26}$$

$$\mathbf{r}_i^{n+1} = \mathbf{r}_i^n + \mathbf{v}_i^{n+\frac{1}{2}} \Delta t \tag{27}$$

The time step was determined using the Courant-Friedrichs-Lewy (CFL) condition to ensure stability:

$$\Delta t \leq 0.25 \left(\frac{h}{c_0}\right) \tag{28}$$

3.9 Algorithm Overview

Upon thoroughly understanding the SPH theory and formalisms, implementation in code is relatively straightforward. While numerous improvements have been developed over time, and parameter values depend on the problem, all SPH algorithms have the same overall structure. A high-level overview can be observed in Figure 6. The neighbourhood search is a critical aspect of SPH simulations as it can considerably reduce the computational cost. While it is possible to exclude this step and iterate over all particles, doing so would be computationally inefficient. The present study employed the KD-Tree algorithm as it was readily available within Python's Scikit-Learn library.
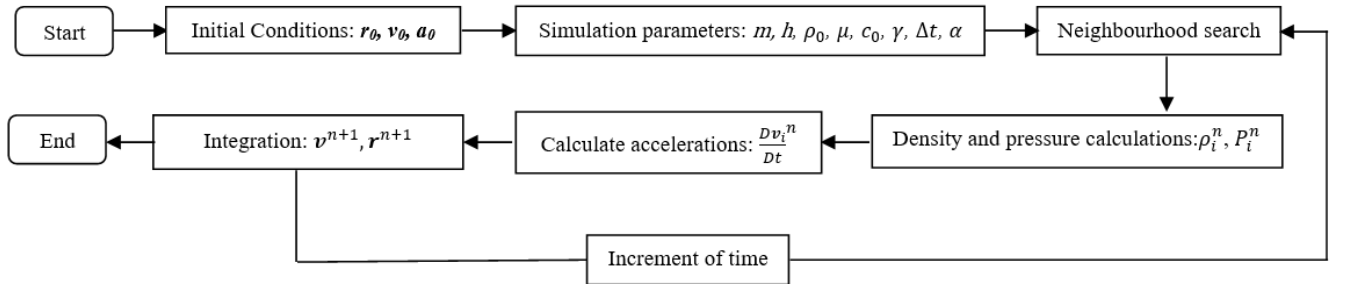

Figure 6: Traditional SPH Algorithm

3.10 XSPH Correction

The XSPH correction, introduced by Monaghan in 1989 [30], eliminates penetration and mixing of particles that occur in traditional SPH while conserving linear and angular momentum. In traditional SPH, two or more particles with different velocities may occupy the same position, potentially causing problems with the simulations. This does not pose a significant concern for low Mach numbers. However, this problem may be amplified in higher velocity flows. The underlying concept of the XSPH correction is to modify the velocity of each particle so that particles in close proximity move with nearly identical velocities. To implement this into the Leapfrog integration scheme, Equation 27 was modified into:

$$\mathbf{r}_i^{n+1} = \mathbf{r}_i^n + \mathbf{v}_i^{n+\frac{1}{2}} \Delta t - \epsilon \sum_j \frac{m_j}{\overline{\rho}_{ij}} \mathbf{v}_{ij}^{n+\frac{1}{2}} W_{ij} \Delta t \tag{29}$$

Where ϵ is a scaling factor usually set to 0.5 [30].

4 Validation and Results

4.1 1D Function Approximations

To give a visualisation of the quality of the discrete approximations of functions using Equations 5 and 6, a simple sine wave, $f(x) = \sin(x)$, and its first-order derivative $f'(x) = \cos(x)$, were approximated for the 1D function benchmark. The cubic spline kernel (Equation 4) was used. 200 equally-spaced particles within a range of 0 to 4π were initially placed, giving $dx = 0.0628$ and $h = 0.0817$. Figure 7(a) shows how the SPH approximations compare to the analytical values and the errors produced.
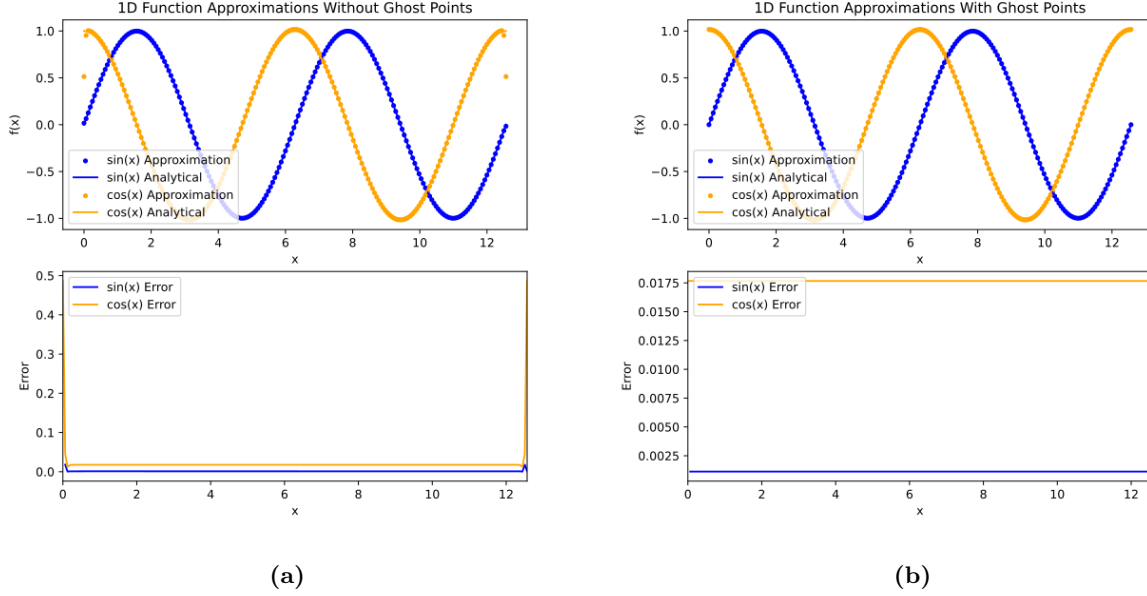

(a)   (b)

Figure 7: 1D Function Approximations (a) Without Ghost Points, (b) With Ghost Points

As seen in Figure 7(a), there is a decreasing approximation quality in the proximity of the domain boundary due to the lack of sampling points outside the domain, illustrated by the approximated points deviating away from the analytical values. The first-order derivative suffers a relatively large error at the boundaries compared to the function approximation, which is one of the drawbacks of SPH. This issue was addressed by adding ghost sampling points outside the edges of the boundary, which are extra sampling points added outside the boundary domain to ensure that each boundary particle has a complete neighbourhood. This is so that the properties carried by the boundary particles are not underestimated. Four ghost points were added to each end of the 1D function with the same initial particle spacing. As seen in Figure 7(b), the errors were significantly reduced.

4.2 2D Dam Break

The classical dam break problem has been used throughout literature to benchmark SPH code and compare the numerical results against experimental results. The initial setup of the problem was derived from the setup by Jančík and Hyhlík [31]. The initial height and width of the liquid column were set to 2m and 1m, respectively. The tank dimensions were 4m wide and 4m tall, consisting of four layers of boundary particles. The overall dynamics of the fluid, until the surge front collides with the right wall, can be seen in Figure 8. An initial particle spacing, dx, of 0.03m was used, giving a total of 2278 fluid particles and 1636 solid particles. The relevant parameters were $\rho_0 = 1000kg/m^3$, $h = 0.039m$, $\alpha = 0.1$ and $dt = 0.000157s$.
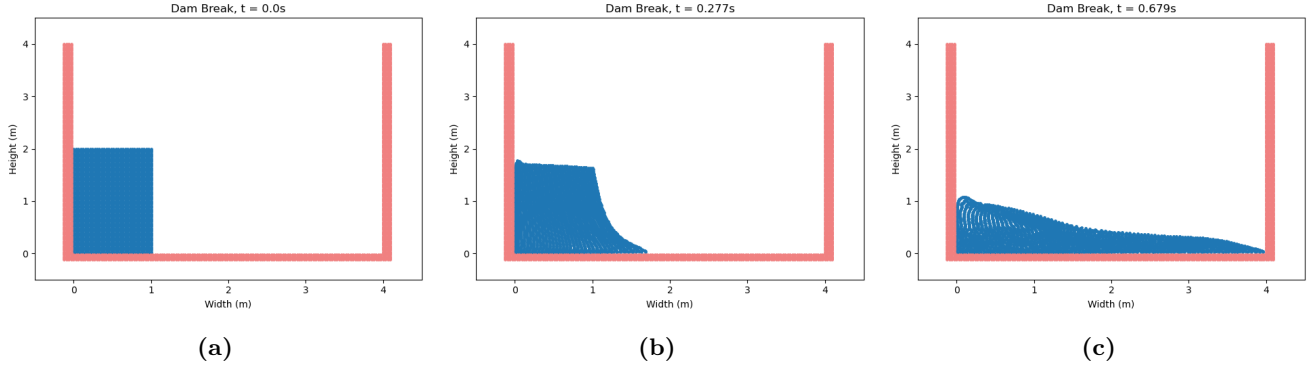
Figure 8: Dam Break Simulation at time (a) t = 0.0s, (b) t = 0.277s and (c) t = 0.679s

The surge front position with respect to time was compared against experimental data conducted by Martin [32] as seen in Figure 9. The variables were normalised and made dimensionless as the containers were different sizes. The dimensionless surge front positions and times are defined as:

$$X = \frac{\zeta}{\zeta_0}, \qquad T = t\sqrt{\frac{2g}{\zeta_0}} \tag{30}$$

Where ζ_0 is the initial liquid column width and ζ is the liquid column width at the current time step. The two experiments conducted by Martin [32] had an initial water column width, ζ_0, of 1.125 inches and 2.25 inches. The height-to-width ratio of the water columns was kept at 2:1 in all instances. Based on Figure 9, the surge front position of the SPH simulation arrived at the edge of the tank first, followed by the experiment with the 1.125-inch water column, then the 2.25-inch column. The discrepancies may be due to errors during the experiments. A more suitable value of α could also be determined for this particular simulation through further tuning. However, the overall results seem to be in good agreement.

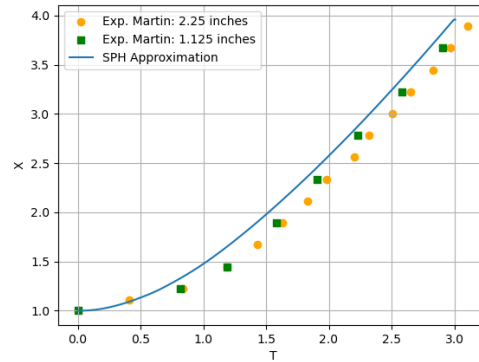**Figure 9:** Dam Break Simulation Results

5 The Swallowing Process

5.1 Modelling the Boundaries

This study obtained processed boundaries from two-dimensional VFSS data from a related investigation, as seen in Figure 10(a). The original VFSS data featured a relatively low frame rate of seven frames per second. As a result, the rapid dynamics and movement of the swallowing process were not adequately captured, with only a limited number of frames available for the segmentation of the bolus and subsequent analysis. In this specific VFSS dataset, the bolus was observable in just three frames, yielding a total

duration of approximately 0.286 seconds. To address the need for finer temporal resolution based on the CFL condition, these three frames were interpolated using the Fourier Descriptor method before being received for this study. This technique generated 800 intermediate frames between each original frame, giving $dt = 0.0001786s$.
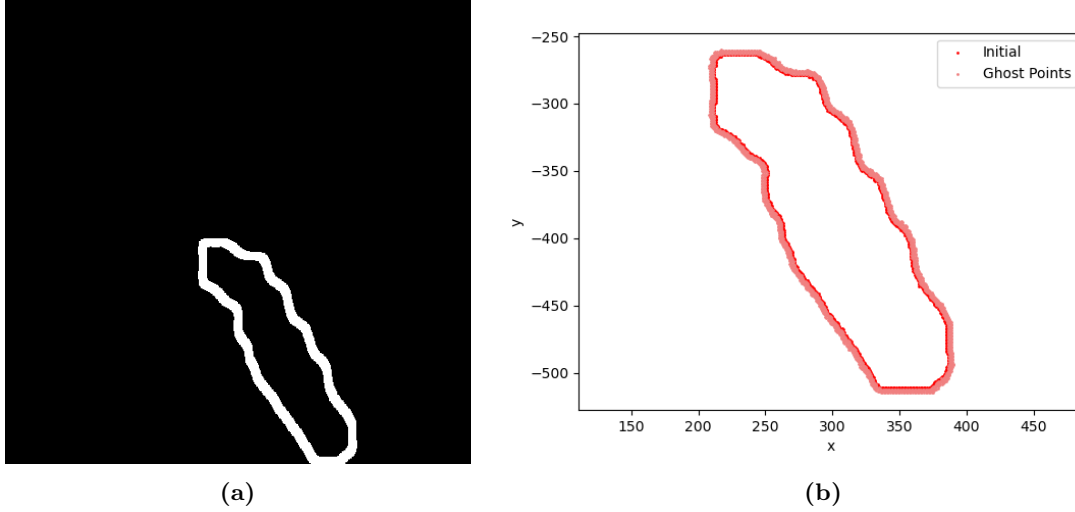

Figure 10: (a) Processed Boundaries, (b) Resampled Boundaries With Ghost Points

To extract the contours from each image and determine the bolus shape at each time step, the *Threshold* and *FindContours* functions from the OpenCV Python library were employed. The extracted outlines were resampled to generate uniformly-spaced points at a predetermined interval, outlining the bolus boundary. Due to the issue of particle deficiency, it was necessary to create four layers of ghost points outside of the boundary, as illustrated in Figure 10(b). Extracting the boundaries this way presented an issue in which the length scale was represented in pixels instead of metres. This affected the length scale in the units and scaled the values of the calculated parameters but did not change the overall physics.

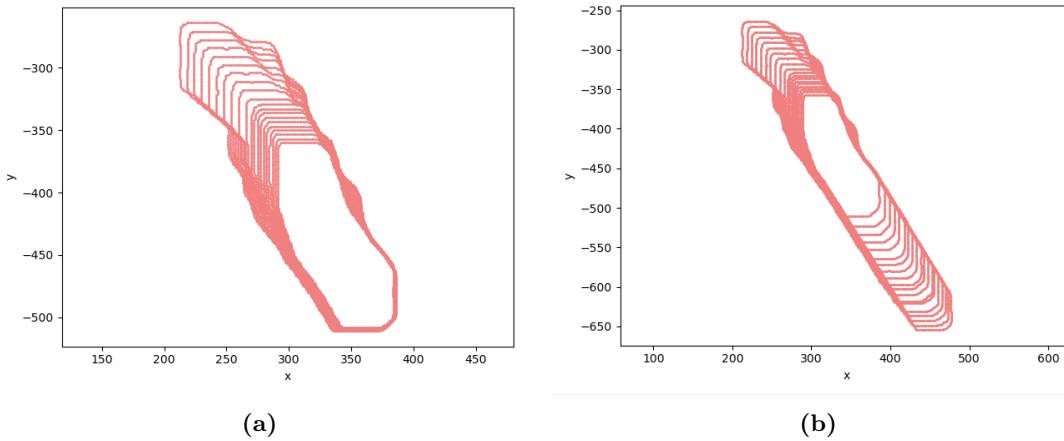## 5.2 Conserving the Bolus Surface Area

Figure 11: Bolus Shape Variation With Time (a) Without Extension and (b) With Extension

From the data obtained, the overall two-dimensional surface area of the bolus decreases over time, with the upper segment of the boundary compressing downwards as illustrated in Figure 11(a). In reality, the

bolus is practically incompressible and its shape changes in three dimensions, which was not captured in this case. To preserve the surface area of the bolus, the bottom segment was artificially extended at each time step by adding a column of particles at the left and right walls and shifting the bottom segment downwards until the initial surface area was reached. However, because of the irregular shape of the bolus, it was challenging to conserve the exact surface area, meaning that it was slightly overestimated at each time step. Figure 11(b) shows how the bolus extends with time.

Once the positions of the boundaries at each time step were initialised, the velocity of each point making up the boundary was calculated. The distance between each point at the current time step and the closest corresponding point at the previous time step was calculated and divided by the time step value. The positions and velocities of the boundaries at each time step were stored for the actual simulation.

5.3   Swallowing Simulation

Using suitable initial parameters was crucial for ensuring the overall stability and precision of the simulation. In this study, it was assumed that the bolus had the properties of water. The relevant parameters were set as follows: $\rho_0 = 1000 kg/m^3$, $\alpha = 0.5$, $dt = 0.0001786s$, $dx = 1.5$ pixels and $h = 1.95$ pixels. Due to the nature of the problem, the reference velocity could not be calculated using Equation 24. Figure 11(a) shows that the upper end of the bolus experienced the most significant change in position. The velocity of the topmost point at each time step was taken, and the mean was computed to determine the reference velocity. This calculation resulted in a velocity of 397.1 pixels per second, which, in turn, yielded an artificial speed of sound, c_0, of 3971 pixels per second.
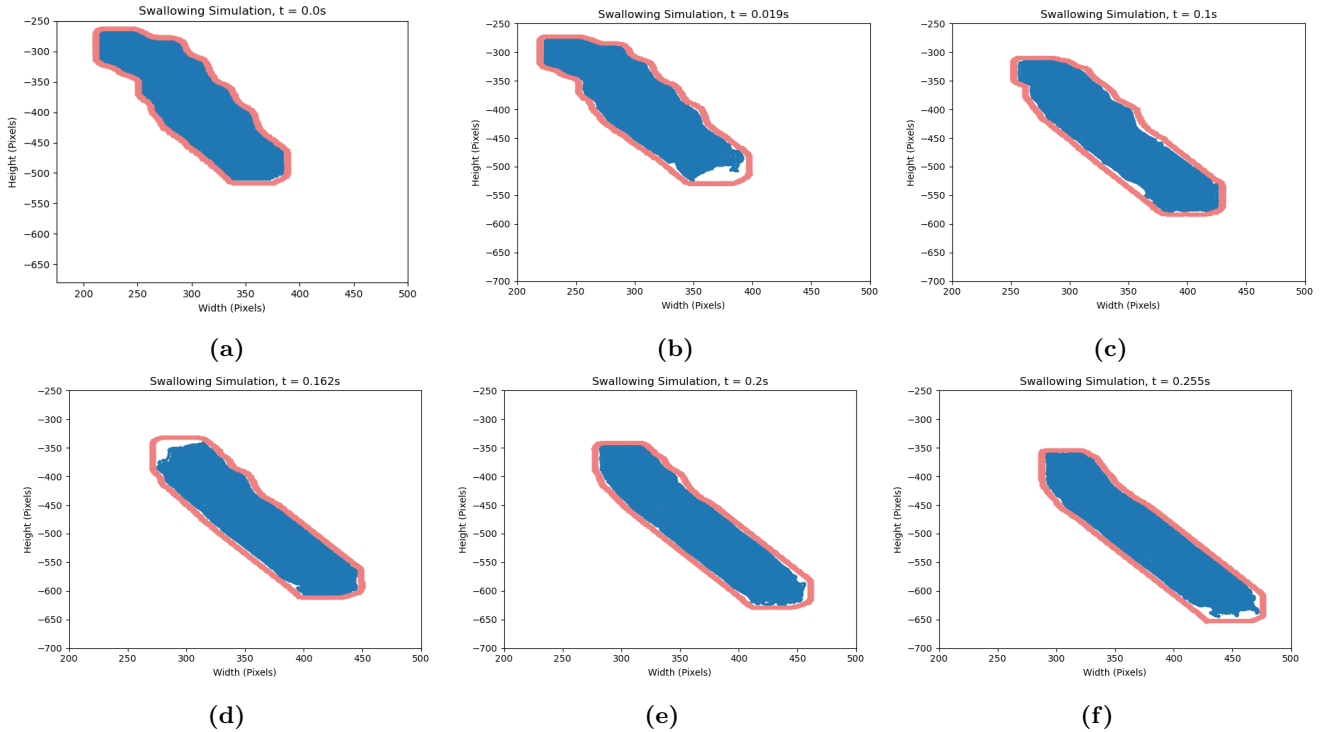

Figure 12: Simulation at (a) t = 0.0s, (b) t = 0.019s, (c) t = 0.1s, (d) t = 0.162s, (e) t = 0.2s and (f) t = 0.255s

The dam break simulation code was adapted for the swallowing simulation by loading the previously saved positions and velocities of the boundaries and updating their values at each time step accordingly. Figure 12 illustrates the overall dynamics of the bolus flow. Figure 12(a) shows that the fluid particles initially conform well to the shape of the boundaries. However, the Weakly Compressible SPH approach used in

this study resulted in some fluid compression, which, coupled with the overestimation of the surface area, led to the formation of an empty space during later time steps.
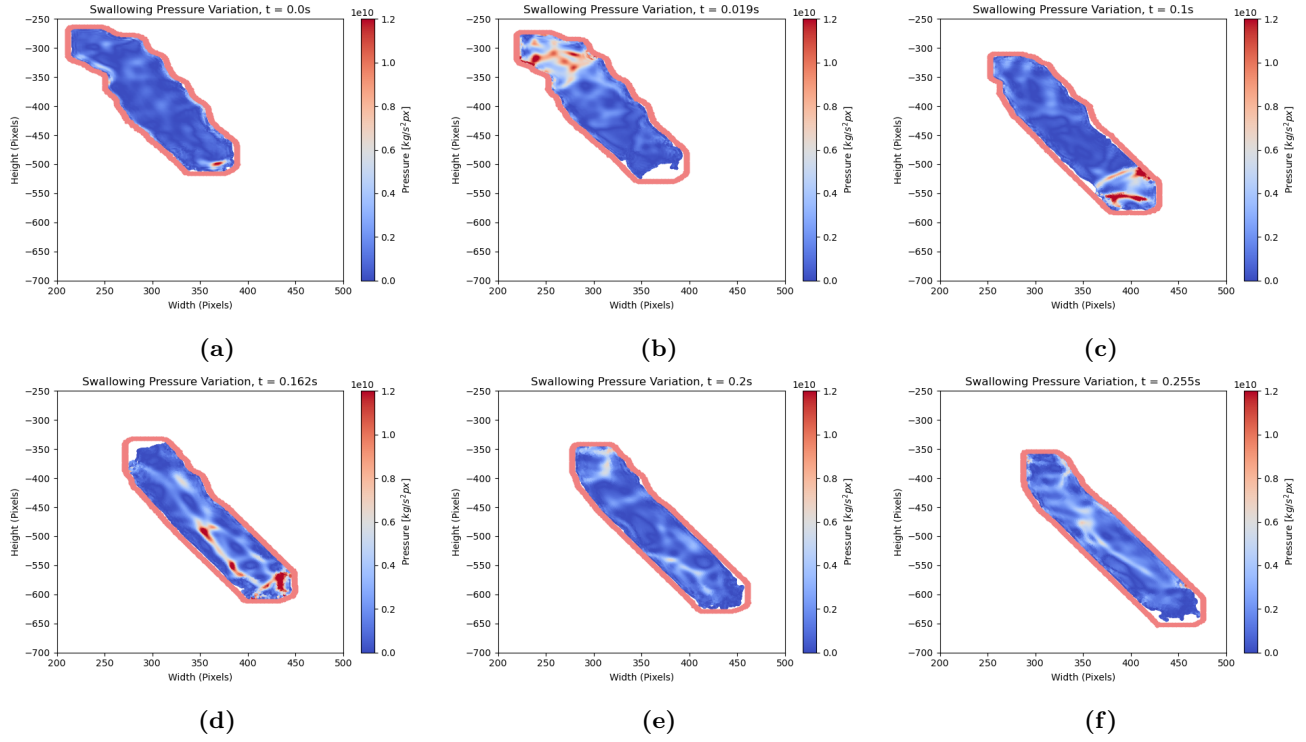

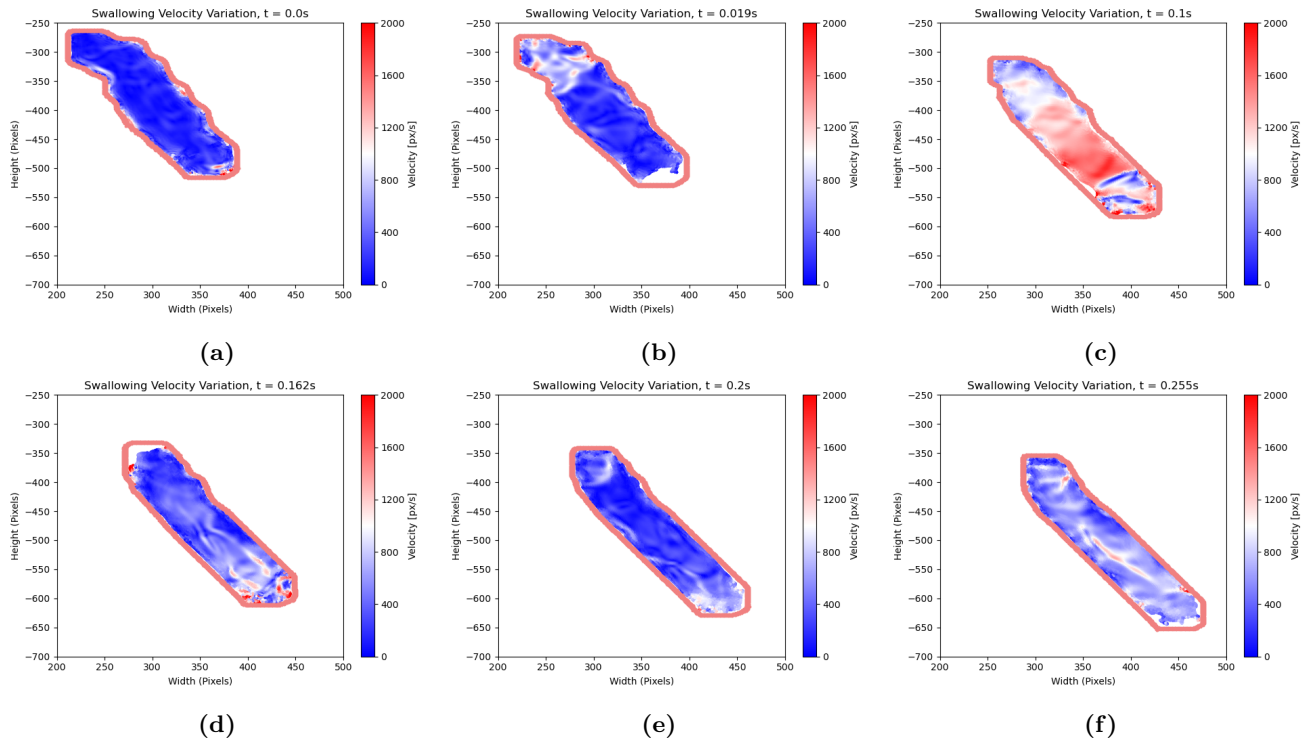**Figure 13:** Pressures at (a) t = 0.0s, (b) t = 0.019s, (c) t = 0.1s, (d) t = 0.162s, (e) t = 0.2s and (f) t = 0.255s

Figure 14: Velocities at (a) t = 0.0s, (b) t = 0.019s, (c) t = 0.1s, (d) t = 0.162s, (e) t = 0.2s and (f) t = 0.255s

Figures 13 and 14 show the overall pressure and velocity dynamics of the bolus flow and how they vary over time. The units shown are not the standard units as the length scale is in pixels (px) instead of metres. The larger pressures at the upper segment of the bolus during earlier time steps, as illustrated in Figure 13(b), could be attributed to the compression of the upper boundary. In earlier time steps, the empty space was present at the bottom segment of the bolus, causing the fluid particles to be forced downwards. Consequently, the fluid particles at the upper segment had relatively higher velocities at earlier time steps. Over time, the empty space shifted toward the sides, and by the 900th time step, it was entirely at the upper segment of the bolus, as illustrated by Figure 13(d) and 14(d), leading to relatively larger pressures and velocities at the bottom segment. The formation of this empty space could most likely result in relatively inaccurate calculations of the parameters, especially at later time steps, highlighting the issue produced by the assumptions made to simulate this process in two dimensions. Despite this, the simulation effectively demonstrated the temporal variation of these parameters, ensuring the stability of the fluid particles and maintaining the integrity of the computational code.

5.4 Discussions and Future Improvements

Although the current two-dimensional simulation has provided valuable insights into the swallowing process, no physical results were available to compare the simulation results. As a result, it was not possible to measure the accuracy and reliability of the simulations. It would be beneficial to incorporate actual medical data, such as those from oesophageal manometry tests, into future work. Oesophageal manometry is a diagnostic tool that measures the pressure and coordination of muscle contractions of the upper aerodigestive tract during swallowing, something that is not captured through VFSS [33]. It is important to note that this test involves inserting a catheter down the throat, which could impact the natural swallowing mechanism and may not always reflect the most accurate and realistic pressure values. Moreover, the length scale of the bolus in the current study was in pixels, resulting in scaled values of the calculated parameters. Scaling down the boundaries according to the actual dimensions of the bolus and normalising the calculated parameters are crucial for directly comparing the simulation results with physical measurements. By validating the simulation results with the data from manometry tests, the fidelity of the simulations could be tested to provide a more comprehensive understanding of the swallowing process.

A significant limitation of the current simulation is the inability to capture the full complexity of the swallowing process, which is inherently an incompressible and three-dimensional phenomenon. As such, future work should focus on developing a three-dimensional model that enforces incompressibility using methods such as Incompressible SPH (ISPH) or Moving Particle Semi-Implicit (MPS) technique to provide more realistic insights into the intricate and multidirectional bolus flow as well as its interactions with the surrounding anatomical structures. Additionally, the implementation of more realistic viscosity formulations that utilise the dynamic or kinematic viscosity of fluids could be a valuable enhancement. This would allow for the realistic modelling of specific fluids such as water or honey.

Instead of segmenting the bolus at each time step, Kikuchi et al. [34] were able to create a geometrically accurate three-dimensional model of the upper aerodigestive tract based on CT scans. They then utilised the MPS method to simulate the bolus flow along the path created. They were able to accurately model the interactions of the bolus with the surrounding tissue and calculate parameter values at each time step when compared to corresponding medical data. However, their model showed some bolus particle penetration into the boundaries. Despite their promising results, there was still a need to improve their simulations, particularly with the forces applied to the bolus particles by the boundaries. It is worth noting that the code created for the simulations in this study is available for public use through the provided link: `https://github.com/imranrizkiputranto/computational-study-of-swallowing-disorders`. This may aid future researchers in their efforts to improve the simulations discussed in this report and build upon the current work to enhance the understanding of the swallowing process.

6   Medical Applications

Early and accurate diagnosis of dysphagia is crucial for implementing appropriate interventions to prevent complications. However, while informative, traditional diagnostic tools such as manometry tests are invasive procedures that involve inserting a tube down the throat. This can be challenging and uncomfortable, particularly for the older population, who are generally more likely to be affected by dysphagia. Ageing often comes with increased sensitivity, reduced tolerance to discomfort, and a higher likelihood of having co-morbidities such as cardiovascular or respiratory diseases that could make invasive procedures riskier and less feasible. Advancements in technology have the potential to help with this. The use of patient-specific data in developing a three-dimensional SPH model would enhance its clinical relevance and applicability. In the current study and the study by Kikuchi et al. [34], the anatomical structures and morphological features of a single person were used to model the boundaries. However, individual variations in anatomy and morphology can significantly affect the swallowing process. Incorporating patient-specific data, such as individualised anatomical measurements and variations in muscle activation patterns, would provide more accurate and personalised simulations. This could potentially aid in developing tailored therapeutic interventions and diagnostic tools for patients with dysphagia.

Image segmentation is a key step in the analysis of medical images. Convolutional neural networks (CNNs) have shown great promise in medical image segmentation tasks due to their ability to learn complex patterns and representations from large datasets. In the context of the present study, CNNs could be trained to segment and extract relevant features from medical images automatically. The combination of deep learning image segmentation and numerical simulations could enable the development of predictive models for swallowing disorders. By training neural networks on large datasets of CT scans and VFSS images in conjunction with numerical simulations, relationships between image features and simulated swallowing parameters could be established.

7   Conclusion

This study demonstrated the potential of applying the SPH method to simulate the human swallowing process. The two-dimensional simulation provided valuable insights into the bolus flow and its interaction with the anatomical structures. However, the current two-dimensional simulation has inherent limitations, such as the inability to capture the full complexity of the swallowing process, which is an incompressible, three-dimensional phenomenon. The assumptions involved in a two-dimensional representation led to relatively inaccurate results. Additionally, the Weakly Compressible SPH approach resulted in some visible fluid compression and challenges related to the conservation of the bolus surface area.

Future work should focus on developing a three-dimensional and incompressible model with improved viscosity formulations which can accurately represent the complex, multidirectional bolus flow and its interaction with the surrounding anatomical structures. Additionally, the incorporation of patient-specific data and advanced image segmentation techniques will be crucial for enhancing the clinical relevance and applicability of the simulations. This would facilitate the development of tailored therapeutic interventions, diagnostic tools, and predictive models for patients with dysphagia, ultimately improving patient outcomes and quality of life.

References

[1] J. Rückert *et al.*, "Functional endoscopy in neurogenic dysphagia: A feasibility study focusing on the esophageal phase of swallowing," *Endoscopy International Open*, vol. 9, pp. 2–3, 2021.

[2] M. A. Nicosia and J. Robbins, "The fluid mechanics of bolus ejection from the oral cavity," *Journal of Biomechanics*, vol. 34, no. 12, pp. 1537–1544, 2001.

[3] M. A. Nicosia, "A planar finite element model of bolus containment in the oral cavity," *Computers in Biology and Medicine*, vol. 37, no. 10, pp. 1472–1478, 2007. QT Variability Heart Rate Variability.

[4] M. Sonomura, H. Mizunuma, T. Numamori, H. Michi-

waki, and K. Nishinari, "Numerical simulation of the swallowing of liquid bolus," *Journal of Texture Studies*, vol. 42, no. 3, pp. 203–211, 2011.

[5] A. Sasegbon and S. Hamdy, "The anatomy and physiology of normal and abnormal swallowing in oropharyngeal dysphagia," *Neurogastroenterology Motility*, vol. 29, pp. 2–4, 2017.

[6] C. Fairfield and R. J. Whittaker, "Mathematical modelling of the normal swallow november 12, 2010 problem presenter :," 2015.

[7] NHS, "Dysphagia (swallowing problems)." `https://www.nhsinform.scot/illnesses-and-conditions/stomach-liver-and-gastrointestinal-tract/dysphagia-swallowing-problems`. Accessed: 01-03-2023.

[8] ASHA, "Adult dysphagia." `https://www.asha.org/practice-portal/clinical-topics/adult-dysphagia/`. Accessed: 01-03-2023.

[9] J. W. Lee, D. R. Randall, L. M. Evangelista, M. A. Kuhn, and P. C. Belafsky, "Subjective assessment of videofluoroscopic swallow studies," *Otolaryngology-Head and Neck Surgery*, vol. 156, pp. 901–905, 2017.

[10] J. C. Rosenbek *et al.*, "A penetration-aspiration scale," *Dysphagia*, vol. 11, pp. 93–98, 1996.

[11] J. A. Logemann, *A Penetration-Aspiration Scale*. Austin: Pro-Ed Inc., 1998.

[12] J. A. Y. Cichero, "Development of international terminology and definitions for texture-modified foods and thickened fluids used in dysphagia management: The iddsi framework," *Dysphagia*, vol. 32, pp. 293–314, 2017.

[13] IDDSI, "Complete iddsi framework detailed definitions." `https://iddsi.org/IDDSI/media/images/Complete_IDDSI_Framework_Final_31July2019.pdf`. Accessed: 26-03-2023.

[14] R. A. Gingold and J. J. Monaghan, "Smoothed Particle Hydrodynamics: Theory and Application to Non-Spherical Stars," *Monthly Notices of the Royal Astronomical Society*, vol. 181, pp. 375–389, 12 1977.

[15] L. B. Lucy, "A numerical approach to the testing of the fission hypothesis.," , vol. 82, pp. 1013–1024, Dec. 1977.

[16] D. Koschier *et al.*, "Smoothed particle hydrodynamics techniques for the physics-based simulation of fluids and solids," 2019.

[17] M. Liu and G. Liu, "Smoothed particle hydrodynamics (sph): an overview and recent developments," *Archives of Computational Methods in Engineering*, vol. 17, pp. 25–76, 03 2010.

[18] Syamsuri *et al.*, "Sph model for interaction of sloshing wave with obstacle in shallow water tank," *Journal of King Saud University - Engineering Sciences*, vol. 34, no. 2, pp. 126–138, 2022.

[19] J. J. Monaghan and J. C. Lattanzio, "A refined particle method for astrophysical problems," *Astronomy and Astrophysics*, vol. 149, pp. 135–143, 1985.

[20] *Post Processing Techniques for Smoothed Particle Hydrodynamics*. PhD thesis.

[21] P. Cossins, "Smoothed particle hydrodynamics," 07 2010.

[22] J. Monaghan, "Simulating free surface flows with sph," *Journal of Computational Physics*, vol. 110, no. 2, pp. 399–406, 1994.

[23] J. P. Morris, P. J. Fox, and Y. Zhu, "Modeling low reynolds number incompressible flows using sph," *Journal of Computational Physics*, vol. 136, no. 1, pp. 214–226, 1997.

[24] J. Monaghan and R. Gingold, "Shock simulation by the particle method sph," *Journal of Computational Physics*, vol. 52, no. 2, pp. 374–389, 1983.

[25] M. Desbrun and M. P. Gascuel, "Smoothed particles: A new paradigm for animating highly deformable bodies," in *Computer Animation and Simulation '96 (Proceedings of EG Workshop on Animation and Simulation*, pp. 61–76, Springer-Verlag, 08 1996.

[26] M. Becker and M. Teschner, "Weakly compressible sph for free surface flows," in *Proceedings of the 2007 ACM SIGGRAPH/Eurographics Symposium on Computer Animation*, SCA '07, (Goslar, DEU), p. 209–217, Eurographics Association, 2007.

[27] A. Danilewicz and Z. Sikora, "Numerical simulation of crater creating process in dynamic replacement method by smooth particle hydrodynamics," *Studia Geotechnica et Mechanica*, vol. 36, 01 2015.

[28] A. J. C. Crespo, M. Gómez-Gesteira, and R. A. Dalrymple, "Boundary conditions generated by dynamic particles in sph methods," *Computers, Materials & Continua*, vol. 5, no. 3, pp. 173–184, 2007.

[29] H. Gotoh and T. Sakai, "Lagrangian simulation of breaking waves using particle method," *Coastal Engineering Journal*, vol. 41, no. 3-4, pp. 303–326, 1999.

[30] J. Monaghan, "On the problem of penetration in particle methods," *Journal of Computational Physics*, vol. 82, no. 1, pp. 1–15, 1989.

[31] P. Jančík and T. Hyhlík, "Simulation of a 2d dam break problem using sph method," 09 2018.

[32] J. C. Martin *et al.*, "Part iv. an experimental study of the collapse of liquid columns on a rigid horizontal plane," *Philosophical Transactions of the Royal Society of London A: Mathematical, Physical and Engineering Sciences*, vol. 244, no. 882, pp. 312–324, 1952.

[33] Mayo Foundation for Medical Education and Research, "Endoscopic mucosal resection." `https://www.mayoclinic.org/tests-procedures/endoscopic-mucosal-resection/about/pac-20385213`, Jun 2022.

[34] T. Kikuchi, Y. Michiwaki, S. Koshizuka, T. Kamiya, and Y. Toyama, "Numerical simulation of interaction between organs and food bolus during swallowing and aspiration," *Computers in Biology and Medicine*, vol. 80, pp. 114–123, 2017.